Adaptive Finite Element and Local Regularization Methods for the Inverse ECG Problem

Christopher R. Johnson
Center for Scientific Computing and Imaging,
Department of Computer Science, University of Utah,
Salt Lake City, Utah 84112 US
E–mail: crj@cs.utah.edu

1 Abstract

One of the fundamental problems in theoretical electrocardiography can be characterized by an inverse problem. We present new methods for achieving better estimates of heart surface potential distributions in terms of torso potentials through an inverse procedure. First, we outline an automatic adaptive refinement algorithm that minimizes the spatial discretization error in the transfer matrix and application of boundary conditions, increasing the accuracy of the inverse solution. Second, we introduce a new local regularization procedure, which works by partitioning the global transfer matrix into sub-matrices, allowing for varying amounts of smoothing. Each submatrix represents a region within the underlying geometric model in which regularization can be specifically 'tuned' using an *a priori* scheme based on the L-curve method. This *local* regularization method can provide a substantial increase in accuracy compared to global regularization schemes. Within this context of local regularization, we show that a generalized version of the singular value decomposition (GSVD) seems to further improve the accuracy of ECG inverse solutions compared to standard SVD and Tikhonov approaches. We conclude with specific examples of these techniques using geometric models of the human thorax derived from MRI data.

2 Introduction

The intrinsic electrical activity of the heart gives rise to electric, and thus potential, fields within the volume of the thorax and upon the torso surface. The fundamental origin of these fields arise from individual cardiac cells receiving electric current from neighboring cells and responding with a local membrane action potential. These cells then inject excitatory current into those neighboring cardiac cells that are not yet excited. High conductivity junctions exist between cardiac cells and provide the intracellular pathway for excitatory currents from activated cells to resting neighbors. An extracellular space provides the return pathway. Viewing a single time instant during the 50–100 ms required for the spread of excitation, the heart can be macroscopically represented as consisting of two regions; one containing already excited cells and the other containing cells still at rest. These two regions are separated by a complex boundary layer of approximately 1 mm thickness, across which, a large (40-80 mV) potential difference occurs. It is this macroscopic distribution of current sources (excited cells) and sinks (resting cells) that forms the time-varying bioelectric source responsible for the electrocardiogram (ECG).

The goal of solving the electrocardiographic inverse problem is to describe bioelectric cardiac sources based on knowledge of the ECG and the volume conductor that surrounds the sources. The necessary elements of such a solution include a quantitative description of the source, the geometry of the volume conductor, and the equations that link source and volume conductor potentials. While a number of different source formulations are possible (see, for example [1], for more details), the literature of the last twenty years has been dominated by two formulations that are based on the electric potentials on the surface of the heart. The first represents the entire cardiac activity by the potential distribution on a closed surface that encloses the heart; while this formulation leads to a unique inverse solution [2], it is, itself, not a unique representation of underlying cardiac sources. However, if the enclosing surface corresponds to the epicardial (outer) surface of the heart, it is possible, albeit very invasive, to measure potentials on this surface and hence both validate and interpret the results. The second formulation arises when we represent the cardiac sources as a uniform, isotropic layer of current dipoles; the layer corresponds, in simplified form, to the boundary between active and resting cells described above. The resulting electrocardiographic potentials then become simple functions of the total spatial solid angle of the excited region, which, in turn, permits a formulation of the inverse problem in terms of the boundary between excited and resting tissue over the entire epicardial (outer) and endocardial (inner) surfaces of the heart. For details of the latter formulation see [3, 4, 5]. In this paper we will focus on the former approach and consider the potentials on the epicardial surface of the heart as an equivalent cardiac source.

With the source determined, our specific inverse problem is to describe potentials on the epicardial surface as a function of those on the surface of the thorax, together with knowledge of the geometric and resistive features of the intervening volume conductor. To describe these relationships mathematically, we begin with a general formulation in terms of the primary current sources within the heart described by Poisson's equation for electrical conduction:

$$\nabla \cdot \sigma \nabla \Phi = -I_v \quad \text{in } \Omega \tag{1}$$

with the boundary condition:

$$\sigma \nabla \Phi \cdot \mathbf{n} = 0 \quad \text{on } \Gamma_T \tag{2}$$

where Φ are the electrostatic potentials, σ is the conductivity tensor, I_v are the cardiac current sources per unit volume, and Γ_T and Ω represent the surface and the volume of the thorax, respectively. While (1) does not have a unique solution, applying additional constraints can produce workable strategies. For example, it is possible to breaks up the volume of the heart into subregions, each with simplifying assumptions regarding the form of discrete sources (*e.g.,* single and multiple current dipoles, quadrupoles, *etc.,*) that approximate local bioelectric sources. The goal then becomes to recover parameters such as the magnitude and direction of the simplified equivalent sources. The difficulty of this approach remains in associating these parameters with underlying physiology so that the resulting inverse solutions are useful (see [6, 7, 8] for a discussion of these points.)

If we now take the approach outlined above and describe the cardiac sources in terms of the epicardial surface potentials, instead of Poisson's equation we solve a generalized Laplace's equation:

$$\nabla \cdot \sigma \nabla \Phi = 0 \tag{3}$$

with Cauchy boundary conditions:

$$\Phi = \Phi_0 \quad \text{on } \Sigma \subseteq \Gamma_T \quad \text{and} \quad \sigma \nabla \Phi \cdot \mathbf{n} = 0 \quad \text{on } \Gamma_T. \tag{4}$$

Solutions to (3 and 4) can be unique and the physical quantities involved are all measurable. However, they share a characteristic of all electrocardiographic inverse problems in that they are ill-posed in the Hadamard sense; *i.e.,* because the solution does not depend continuously on the data, small errors in the measurement of the torso potentials or thorax geometry can yield unbounded errors in the solution. The origins of this ill-posedness are biophysical and lie in the attenuation of potentials as we move away from the source and the fact that the potential at any point on the torso surface is a weighted superposition of all the individual sources within the heart. Hence, the ECG represents an integration of many sources, the influence of each of which decreases sharply with distance. To solve the inverse solution, we must perform the complementary operations of amplification and differentiation on the ECG, but also on the inevitable noise that accompanies it. The result is exquisite sensitivity to any fluctuations in the input signals or geometric models.

Dealing with the ill-posed nature of the inverse problem has become the primary goal of a great deal of recent research in inverse problems as it remains the single largest obstacle to medical implementation. The most common approach is to apply constraints to the inverse solution in order to reduce its dependence on boundary conditions. The points of difficulty lie in the choice of constraints and the corresponding weight each receives in determining the best—in whatever sense we wish to define "best"—solution. Examples of recent specific approaches include constraints that change in time [9], constraints that change in space [10, 11, 12], multiple simultaneous constraints [13, 14], and methods by which to determine best constraint weighting from the available *a priori* information [15, 16] (see [17] for a recent review).

In this paper, we describe some recent progress in two facets of the inverse problem. The first deals with improvements in the numerical techniques required to solve both the electrocardiographic forward and inverse problems when using realistic geometries. With this technique, we adjust the spatial resolution of the discrete geometry mesh in a way that reflects the estimated local error in the forward or inverse problem. The second aspect of the inverse problem we address is a form of applying constraints to the ill-conditioned discrete inverse problem to "regularize" the solution and restore continuity of the solution back onto the data. Our specific contribution lies in varying the degree of regularization constraint according to the degree of *local* ill-posedness. We show how application of these technique to a two-dimensional inverse problem can achieve noteworthy improvements in solution accuracy.

A major motivation for solving the inverse problem in electrocardiography lies in its immense clinical utility for the diagnosis and treatment of some of our most frequent and lethal health conditions. Accurate inverse solutions would improve the non-invasive evaluation of myocardial ischemia and infarcts [18], the localization of ventricular arrhythmias [19], the site of accessory pathways in Wolff-Parkinson-White (WPW) syndrome [20], and, more generally, the determination of patterns of the spread of excitation and repolarization in the heart.

3 Mathematical Theory

3.1 Finite Element Approximation

In order to solve the boundary value problem in (1) or (3) in terms of the epicardial potentials, we need to pose the problem in a computationally tractable way. This involves approximating the boundary value problem on a finite dimensional subspace and reformulating it in terms of a linear matrix equation—finding the forward solution that corresponds to the specific inverse problem we wish to solve. For this study we utilized the finite element method (FEM) to approximate the field equation and construct the set of matrix equations, the solution to which is a transform matrix that is the forward solution. Briefly, one starts with the Galerkin formulation of (1). Note that this includes the Dirichlet and Neumann boundary conditions,

$$(\sigma \nabla \Phi, \nabla \overline{\Phi}) = -(I_v, \overline{\Phi}), \tag{5}$$

where $\overline{\Phi}$ is an arbitrary test function, which can be thought of physically as a virtual potential field, and the notation $(\phi_1, \phi_2) \equiv \int_\Omega \phi_1 \phi_2 \; d\Omega$ denotes the inner product in $L_2(\Omega)$. We now use the finite element method to turn the continuous problem into a discrete formulation. First we discretize the solution domain, $\Omega = \bigcup_{e=1}^{N} \Omega_e$, and define a finite dimensional subspace, $V_h \subset V = \{\overline{\Phi} : \overline{\Phi}$ is continuous on Ω, $\nabla \overline{\Phi}$ is piecewise continuous on $\Omega\}$. We define parameters of the function $\overline{\Phi} \in V_h$ at node points, $\alpha_i = \overline{\Phi}(x_i), i = 1, 2, \ldots, N$ and define the basis functions $\Psi_i \in V_h$ as linear piecewise continuous functions that take the value 1 at node points and 0 elsewhere. We can then represent the function, $\overline{\Phi} \in V_h$ as:

$$\overline{\Phi} = \sum_{i=1}^{N} \alpha_i \Psi(x_i) \tag{6}$$

such that $\overline{\Phi} \in V_h$ can be written in a unique way as a linear combination of the basis functions $\Psi_i \in V_h$. The finite element approximation of the original boundary value problem (1) can be stated as:

$$\text{Find } \Phi_h \in V_h \text{ such that } (\sigma \nabla \Phi_h, \nabla \overline{\Phi}) = -(I_v, \overline{\Phi}). \tag{7}$$

Furthermore, since $\Phi_h \in V_h$ satisfies (7), then we have $(\sigma \nabla \Phi_h, \nabla \Psi) = -(I_v, \Psi_i)$. Finally, since Φ_h itself can be expressed as the linear combination:

$$\Phi_h = \sum_{i=1}^{N} \xi_i \Psi_i(x) \quad \xi_i = \Phi_h(x_i), \tag{8}$$

we can then write (7) as:

$$\sum_{i=1}^{N} \xi_i (\sigma_{ij} \nabla \Psi_i, \nabla \Psi_j) = -(I_v, \Psi_j) \quad j = 1, \ldots, N. \tag{9}$$

The finite element approximation of (1) can equivalently be expressed as a system of N equations with N unknowns, $\xi_1, \ldots, \xi_N$ (the electrostatic potentials at the nodes in the domain). In matrix form, the above system is expressed as $A\xi = b$, where $A = (a_{ij})$ is the global stiffness matrix and has elements $(a_{ij} = (\sigma_{ij} \nabla \Psi_i, \nabla \Psi_j))$, while $b_i = -(I_v, \Psi_i)$ is the vector of source contributions.

3.1.1 Application of the FE Method for 3-D Domains

We now illustrate the concepts of the Finite Element Method by considering the solution of (3) using linear three-dimensional elements. We start with a 3D domain Ω which represents the geometry of our volume conductor and break it up into discrete elements to form a finite dimensional subspace, Ω_h. For 3D domains we have the choice of representing our function as either tetrahedra,

$$\tilde{\Phi} = \alpha_1 + \alpha_2 x + \alpha_3 y + \alpha_4 z, \tag{10}$$

or hexahedra,

$$\tilde{\Phi} = \alpha_1 + \alpha_2 x + \alpha_3 y + \alpha_4 z + \alpha_5 xy + \alpha_6 yz + \alpha_7 xz + \alpha_8 xyz. \tag{11}$$

Because of space limitations we restrict our development to tetrahedra, knowing that it is easy to modify our formulae for hexahedra. We take out a specific tetrahedra from our finite dimensional subspace and apply the previous formulations for the four vertices,

$$\begin{pmatrix} \tilde{\Phi}_1 \\ \tilde{\Phi}_2 \\ \tilde{\Phi}_3 \\ \tilde{\Phi}_4 \end{pmatrix} = \begin{pmatrix} 1 & x_1 & y_1 & z_1 \\ 1 & x_2 & y_2 & z_2 \\ 1 & x_3 & y_3 & z_3 \\ 1 & x_4 & y_4 & z_4 \end{pmatrix} \begin{pmatrix} \alpha_1 \\ \alpha_2 \\ \alpha_3 \\ \alpha_4 \end{pmatrix}, \tag{12}$$

or

$$\tilde{\Phi}_{\mathbf{i}} = \mathbf{C}\alpha, \tag{13}$$

which define the coordinate vertices, and

$$\alpha = \mathbf{C}^{-\mathbf{1}}\tilde{\Phi}_{\mathbf{i}} \tag{14}$$

which defines the coefficients. From equations (10) and (14) we can express $\tilde{\Phi}$ at any point within the tetrahedra,

$$\tilde{\Phi} = [1, x, y, z]\alpha = \mathbf{S}\alpha = \mathbf{S}\mathbf{C}^{-\mathbf{1}}\tilde{\Phi}_{\mathbf{i}} \tag{15}$$

or, most succinctly,

$$\tilde{\Phi} = \sum_i N_i \tilde{\Phi}_i. \tag{16}$$

$\tilde{\Phi}_i$ is the solution value at node i, and $\mathbf{N} = \mathbf{S}\mathbf{C}^{-\mathbf{1}}$ is the local *shape function* or *basis function*. This can be expressed in a variety of ways in the literature (depending, usually, on whether you are reading engineering or mathematical treatments of finite element analysis):

$$\Phi_j(N_i) = N_i(x, y, z) = f_i(x, y, z) \equiv \frac{a_i + b_i x + c_i y + d_i z}{6V} \tag{17}$$

where

$$6V = \begin{vmatrix} 1 & x_1 & y_1 & z_1 \\ 1 & x_2 & y_2 & z_2 \\ 1 & x_3 & y_3 & z_3 \\ 1 & x_3 & y_3 & z_4 \end{vmatrix} \tag{18}$$

defines the volume V of the tetrahedra.

Now that we have a suitable set of basis functions, we can find the finite element approximation to our 3D problem. Our original problem can be formulated as

$$a(u,v) = (I_v, v) \quad \forall v \in \Omega, \tag{19}$$

where

$$a(u,v) = \int_\Omega \nabla u \cdot \nabla v d\Omega \tag{20}$$

and

$$(I_v, v) = \int_\Omega I_v \cdot v d\Omega. \tag{21}$$

The finite element approximation to the original boundary value problem is

$$a(u_h, v) = (I_v, v) \quad \forall v \in \Omega_h, \tag{22}$$

which has the equivalent form

$$\sum_{i=1}^{N} \xi_i a(\Phi_i, \Phi_j) = (I_v, \Phi_j), \tag{23}$$

where

$$a(\Phi_i, \Phi_j) = a(\Phi_i(N_j), \Phi_j(N_i)), \tag{24}$$

which can be expressed by the matrix and vector elements

$$(a_{ij}) = \int_{\Omega_E} (\frac{\partial N_i}{\partial x}\frac{\partial N_j}{\partial x} + \frac{\partial N_i}{\partial y}\frac{\partial N_j}{\partial y} + \frac{\partial N_i}{\partial z}\frac{\partial N_j}{\partial z}) d\Omega \tag{25}$$

and

$$I_i = \int_{\Omega_E} N_i I_v \, d\Omega. \tag{26}$$

Fortunately, the above quantities are easy to evaluate for linear tetrahedra. As a matter of fact, there are closed form solutions for the matrix elements (a_{ij}):

$$\int_{\Omega_h} N_1^a N_2^b N_3^c N_4^d \, d\Omega = 6V \frac{a!b!c!d!}{(a+b+c+d+3)!}. \tag{27}$$

Therefore,

$$(a_{ij}) = \int_{\Omega_E} \frac{b_i b_j + c_i c_j + d_i d_j}{6V^2}\, d\Omega = \frac{b_i b_j + c_i c_j + d_i d_j}{6V}, \tag{28}$$

and, for the right hand side, we have, assuming constant sources,

$$I_i = \int_{\Omega_E} \frac{a_i + b_i x + c_i y + d_i z}{6V} I_v \, d\Omega = \frac{V I_v}{4}. \tag{29}$$

which have the compact forms

$$a_{ij}^{(n)} = \frac{1}{6V}(b_i^{(n)} b_j^{(n)} + c_i^{(n)} c_j^{(n)} + d_i^{(n)} d_j^{(n)}) \tag{30}$$

and

$$I_i^{(n)} = \frac{V I_v}{4} \quad \text{for constant sources.} \tag{31}$$

Now we add up all the contributions from each element into a global matrix and global vector.

$$\sum_{n=1}^{Nel} (a_{ij}^{(n)})(\xi_i) = (I_i^{(n)}) \tag{32}$$

where Nel is equal to the total number of elements in the discretized solution domain and i represents the node numbers (vertices). This yields a linear system of equations of the form $\mathbf{A}\Phi = \mathbf{b}$, where Φ is our solution vector of voltages, $\mathbf{A}$ represents the geometry and conductivity of our volume conductor, and $\mathbf{b}$ represents the contributions from the current sources and boundary conditions.

Within the finite element method, the Neumann boundary condition

$$\nabla \Phi \cdot \mathbf{n} = 0 \tag{33}$$

is satisfied automatically within the Galerkin and variational formulations. This can be seen by using Green's divergence theorem,

$$\int_{\Omega} \nabla \cdot \mathbf{A} dx = \int_{\Gamma} \mathbf{A} \cdot \mathbf{n} \, dS, \tag{34}$$

and applying it to the left hand side of the Galerkin finite element formulation:

$$\int_\Omega \nabla v \cdot \nabla w \, d\Omega \equiv \int_\Omega [\frac{\partial v}{\partial x_1}\frac{\partial w}{\partial x_1} + \frac{\partial v}{\partial x_2}\frac{\partial w}{\partial x_2}] \, d\Omega$$
$$= \int_\Gamma [v\frac{\partial w}{\partial x_1} n_1 + v\frac{\partial w}{\partial x_2} n_2] \, dS - \int_\Omega v[\frac{\partial^2 w}{\partial x_1^2} + \frac{\partial^2 w}{\partial x_2^2}] \, d\Omega$$
$$= \int_\Gamma v\frac{\partial w}{\partial n} \, dS - \int_\Omega v\nabla^2 w \, d\Omega. \qquad (35)$$

If we multiply our original differential equation, $\nabla^2\Phi = -I_v$, by an arbitrary test function and integrate, we obtain

$$(I_v, v) = -\int_\Omega (\nabla^2\Phi) v \, d\Omega = -\int_\Gamma \frac{\partial \Phi}{\partial n} v \, dS + \int_\Omega \nabla\Phi \cdot \nabla v \, d\Omega = a(\Phi, v), \qquad (36)$$

where the boundary integral term, $\frac{\partial\Phi}{\partial n}$ vanishes and we obtain the standard Galerkin finite element formulation.

To apply the Dirichlet condition, we have to work a bit harder. To apply the Dirichlet boundary condition directly, one usually modifies the (a_{ij}) matrix and b_i vector such that one can use standard linear system solvers. This is accomplished by implementing the following steps.

Assuming we know the ith value of u_i,

1. Subtract from the ith member of the r.h.s. the product of a_{ij} and the known value of Φ_i (call it $\bar{\Phi}_i$, this yields the new right hand side, $\hat{b}_i = b_i - a_{ij}\bar{\Phi}_j$.
2. Zero the ith row and column of A: $\hat{a}_{ij} = \hat{a}_{ji} = 0$.
3. Assign $\hat{a}_{ii} = 1$.
4. Set the jth member of the r.h.s. equal to $\bar{\Phi}_i$.
5. Continue for each Dirichlet condition.
6. Solve the augmented system, $\hat{A}\Phi = \hat{b_v}$.

3.1.2 Applications of the FE Method for 2-D Domains

Since we show initial results within two-dimensional domains, we briefly comment on the reduction of the three-dimensional case for tetrahedra to the two-dimensional case for triangles.

The reduction to two-dimensional triangular domains from the presentation given above for three-dimensional tetrahedral domains is very straightforward. Specifically, one can substitute the representation below of a linear triangle for the representation of the tetrahedra in equation (10)

$$u \approx \tilde{\Phi} = \alpha_1 + \alpha_2 x + \alpha_3 y \tag{37}$$

Following the development from equations (12 – 16), the two-dimensional linear basis function for the triangle would be defined by (in place of equation (17))

$$\Phi_j(N_i) = N_i(x,y) = f_i(x,y) \equiv \frac{a_i + b_i x + c_i y}{2A} \tag{38}$$

where A is the area of the triangle,

$$A = \frac{1}{2} \begin{vmatrix} 1 & x_1 & y_1 \\ 1 & x_2 & y_2 \\ 1 & x_3 & y_3 \end{vmatrix}. \tag{39}$$

This yields matrix elements,

$$(a_{ij}) = \int_{\Omega_E} (\frac{\partial N_i}{\partial x}\frac{\partial N_j}{\partial x} + \frac{\partial N_i}{\partial y}\frac{\partial N_j}{\partial y}) d\Omega \tag{40}$$

with similar formulas to equations (27–28) for the evaluation of these elements for linear triangles:

$$\int_{\Omega_h} N_1^a N_2^b N_3^c \, d\Omega = 2A \frac{a!b!c!}{(a+b+c+2)!}, \tag{41}$$

such that,

$$(a_{ij}) = \int_{\Omega_E} \frac{b_i b_j + c_i c_j}{4A^2} \, d\Omega = \frac{b_i b_j + c_i c_j}{4A}. \tag{42}$$

We can then follow the same implementation strategy for the application of the Neumann and Dirichlet boundary conditions as with the tetrahedral elements.

Background information on finite element methods can be found in [21, 22, 23, 24]

3.2 Adaptive Methods

Solving either Poisson's or Laplace's equation by any of the standard methods (finite element, boundary element, or finite difference) for realistic shapes requires the use of discrete geometric models. Both the lack of clear relationships between level of discretization and solution accuracy as well as the large computational and manual cost of creating geometric models has lead many researchers to select approximately constant sized elements throughout the geometric models. The size and configuration of these elements also usually remain constant not only over space, but also over time, independent of any changes in the cardiac potentials.

We have found, however, that by using *a posteriori* estimates from the finite element approximation of the governing equations, along with a minimax theorem to determine the stopping criterion, we can locally refine the discretization and reduce the errors in the forward solution. A novel aspect of our approach is that it uses local approximations of the error in the numerical solutions to drive an automatic adaptive mesh refinement [25, 26].

It has always been assumed that improving the accuracy of the forward solution also improves the subsequent inverse solution. This seems to be true up to a point since further refinement increases the number of degrees of freedom and correspondingly increases the condition number of the transfer matrix. Finding the "optimal" point at which the added degrees of freedom stop increasing the accuracy of the inverse solution is an open research problem.

Mathematically, we can obtain an error estimator by starting from the *weak formulation* of the finite element approximation, (7). We can prove that $\Phi_h \in V_h$ (where Φ_h is the finite element solution and related to ξ by (8)) is the best approximation of the exact solution Φ in the sense that

$$\|\nabla\Phi \; - \; \nabla\Phi_h\| \;\leq\; \|\nabla\Phi \; - \; \nabla\tilde{\Phi}\| \quad \forall\, \tilde{\Phi} \in V_h \tag{43}$$

where

$$\|\nabla\tilde{\Phi}\| \;=\; \left(\int_\Omega \nabla\tilde{\Phi}\cdot\nabla\tilde{\Phi}\right)^{\frac{1}{2}}. \tag{44}$$

In particular, we can choose $\tilde{\Phi}$ to be the interpolant of Φ

$$\pi_h\Phi(N_i) \;=\; \Phi(N_i) \qquad i \;=\; 1,\ldots,M \qquad \pi_h\Phi \in V_h. \tag{45}$$

This says that the error in the finite element approximation is bounded from above by the interpolation error. With certain constraints on our elements, we can prove the following, well know relationships:

$$\|\nabla\Phi \;-\; \nabla\pi_h\Phi\| \;\leq\; Ch \tag{46}$$

and

$$\|\Phi \;-\; \pi_h\Phi\| \;\leq\; Ch^2 \tag{47}$$

where C is a positive constant that depends on the size of the second partial derivative of Φ and the smallest angle formed by the sides of the elements in V_h. These estimates show that the error in both Φ and $\nabla\Phi$ tend to zero as the discretization parameter, h, tends to zero. We can use these relationships to provide an adaptive algorithm for decreasing discretization error.

More precisely, we define the semi-norm:

$$|\tilde{\Phi}|_{H^r(\Omega)} \;=\; \left(\sum_{|\alpha|=r} \int_\Omega |D^\alpha \tilde{\Phi}|^2 \, dx\right)^{\frac{1}{2}} \tag{48}$$

where

$$D^\alpha \tilde{\Phi} \;=\; \frac{\partial^{|\alpha|}\tilde{\Phi}}{\partial x_1^{\alpha_1} \partial x_2^{\alpha_2}} \qquad |\alpha| \;=\; \alpha_1 \;+\; \alpha_2 \tag{49}$$

are α-order partial derivatives and

$$H^K(\Omega) = \{\tilde{\Phi} \in L_2(\Omega) : \; D^\alpha \tilde{\Phi} \in L_2(\Omega), \; |\alpha| \leq K\} \tag{50}$$

defines the Sobolev spaces. Given these definitions, we can then obtain the error estimates analogous to those in (46) and (47) for the finite element approximation [27, 22]:

$$|\Phi - \Phi_h|_{H^1(\Omega)} \;\leq\; |\Phi - \pi_h\Phi|_{H^1(\Omega)} \;\leq\; C \left[\sum_{K \in T_n} \left(h_k |\Phi|_{H^2(K)}\right)^2\right]^{\frac{1}{2}} \tag{51}$$

or, in the $L_2(\Omega)$ norm,

$$\|\Phi - \Phi_h\|_{L_2(\Omega)} \;\leq\; \|\Phi - \pi_h\Phi\|_{L_2(\Omega)} \;\leq\; Ch^2 |\Phi|_{H^2(\Omega)}. \tag{52}$$

For the potential gradients we have [28]:

$$\begin{aligned}\|\nabla\Phi - \nabla\Phi_h\|_{L_\infty(\Omega)} &\leq C\|\nabla\Phi - \nabla\pi_h\tilde{\Phi}\|_{L_\infty(\Omega)} \\ &\leq C\max[h_K \max_{\alpha=2}\|D^\alpha\Phi\|_{L_\infty(\Omega)}].\end{aligned} \tag{53}$$

Given these previous error estimates for the finite element approximation, we can now use the estimates to decide where in our original finite element mesh the approximation is not accurate and create a recursive, adaptive algorithm to re-discretize in the appropriate areas. Suppose we want the accuracy of our finite element approximation to be within some given tolerance, δ, of the true solution, i.e.

$$|\Phi - \Phi_h|_{H^1(\Omega)} \ \leq \ \delta. \tag{54}$$

Then, we refine our mesh until,

$$\sum_{K\in T_h} (h_k|\Phi_h|_{H^2(K)})^2 \ \leq \ \frac{\delta^2}{C^2}. \tag{55}$$

Here the sum is over all the K elements in the tessellated geometry, T_h, and we test to see if the error is less than the *normalized* tolerance. If the value of the error estimate exceeds the tolerance, the element is ‘flagged’ for further refinement. The refinement can occur either by further subdividing the egregious element (so-called h-adaption) or by increasing the order of the basis function of the element (p-adaption), or both (hp-adaption). One should note that the $H^2(\Omega)$ norm in (55) requires the second partial derivative of the finite element approximation. As stated in (8), we have assumed a linear basis function for our fundamental element. Thus, there is no continuity of the second derivative and we must approximate it using a centered difference (or other) formula based on first derivative information.

Of significant practical importance is the choice of a reasonable tolerance, δ. Since the general location and bounds of the potential field are dictated by known physiological considerations, we can generate an initial mesh based upon simple field strength-distance arguments. To estimate an upper bound of the potential (or electric) field we can compute the field strength analytically on a cylindrical surface that encloses the actual thorax geometry. The result is an estimate of the potential field and potential gradients that we then use to produce the initial graded mesh. The goal of this calculation is to assure that the errors far from the sources are minimal. We can then refine our finite element mesh by choosing the tolerance, δ, to be some fraction of the estimated error corresponding to the elements furthest from the sources. Thus we have used a minimax principle, minimizing the maximum error based upon initial (conservative) estimates of the potential field and potential gradients [25].

3.2.1 Adaptive hp Methods

While Szabo pioneered the method of *hp* adaptive finite element methods in the early 1970s, and their use is widespread among the computational fluid dynamics and solid mechanics communities, the use of such methods have basically been non-existent within the bioelectric field community. One reason for this is probably due to the fact that most early *hp* methods for volumetric domains used systems of structured elements. Given the complex geometry of the human torso, such methods were difficult to implement.

More recently, non-conforming formulations have been developed to allow greater flexibility in handling geometric complexities [29, 30, 31]. However, such algorithms could be difficult to implement computationally since new functions needed to be created for each basis function. This was especially true for three-dimensional geometries that utilized high order basis functions. Within the past few years, however, researchers have developed new computationally efficiently hierarchical bases that lead to a better conditioning of the stiffness matrix and thus allow for fast iterative algorithms to be effectively employed in the solution of the resulting linear system [32].

We will give an example of the use of a high order *hp* finite element to the inverse ECG problem. Following the work work by [32, 33], we define a polynomial basis, denoted by ${}^{1-2_k}g_{lm}(r,s)$ so we can approximate the function $f(x,y)$ by a C^0 continuous expansion over K triangles in the form:

$$f(x,y) = \sum_k \sum_l \sum_m \overline{f}^k_{lmn} \; {}^{1-2_k}g_{lm}(r(x,y), s(x,y)). \tag{56}$$

Here $\overline{f}^k_{lmn}$ is the expansion coefficient corresponding to the expansion polynomial ${}^{1-2_k}g_{lm}(r,s)$ in the kth triangular element. (x,y) are the global spatial coordinates of the function and (r,s) are the local coordinates within any given triangle. The basis is now split into interior, vertex, and edge modes. The interior modes are zero on the triangular boundary. The vertex modes vary linearly from a unit value at one vertex to zero at the others. The edge modes only have magnitude along one edge and are zero at all

other vertices and edges. Using area coordinates-ordinates, such that any point in the triangle can be described by three coordinates-ordinates L_1, L_2 and L_3 (which can be interpreted as the ratio of the areas A_1, A_2 and A_3 such that $A = A_1 + A_2 + A_3$), we can express the split of the basis in the following way.
Vertex modes

$$ {}^{1-2^{vertA}}g_{10} = L_1 \tag{57}$$

$$ {}^{1-2^{vertB}}g_{10} = L_2 \tag{58}$$

$$ {}^{1-2^{vertC}}g_{01} = L_3 \tag{59}$$

Edge modes $(2 \leq l;\, 1 \leq m \,|\, l < L;\, l + m < M))$

$$ {}^{1-2^{side1}}g_{l0} = L_1 L_2 P^{1,1}_{l-2} \frac{L_2 - L_1}{1 - L_3}(1 - L_3)^{l-2} \tag{60}$$

$$ {}^{1-2^{side2}}g_{1m} = L_2 L_3 P^{1,1}_{m-1}(2L_3 - 1) \tag{61}$$

$$ {}^{1-2^{side3}}g_{1m} = L_1 L_3 P^{1,1}_{m-1}(2L_3 - 1) \tag{62}$$

Interior modes $(2 \leq l;\, 1 \leq m \,|\, l < L;\, l + m < M))$

$$ {}^{1-2^{interior}}g_{lm} = L_1 L_2 L_3 P^{1,1}_{l-2} \frac{L_2 - L_1}{1 - L_3}(1 - L_3)^{l-2} P^{2l-1,1}_{m-1}(2L_3 - 1) \tag{63}$$

Where $P_n^{\alpha,\beta}(x)$ is the nth-order Jacobi polynomial in the interval $[-1, 1]$ with the orthogonality relationship

$$ \int_{-1}^{1} P_l^{\alpha,\beta}(x) P_m^{\alpha,\beta}(x)(1 - x)^{\alpha}(1 + x)^{\beta} dx = \delta_{lm} \tag{64}$$

The latest computationally efficient adaptive finite elements methods are so-called spectral/hp element methods [33]. Thus far, such methods have not been used in bioelectric field simulation, however, their use may be very appropriate for large-scale models with complex geometries. For those unfamiliar with adaptive methods, additional information may be found in [34, 35, 36, 37].

3.3 Regularization

Traditional schemes for solving the inverse problem, (3), have involved reformulating the linear equation, $A\xi = b$, into $\xi_T = K\xi_E$, where ξ_T and ξ_E are the voltages on the body surface (torso) and heart's surface (epicardium) respectively, and K is the $T \times E$ transfer matrix of coefficients relating the measured torso voltages to the voltages measured on the heart. From this statement of the forward problem, the inverse problem can then be expressed as $\xi_E = K^{-1}\xi_T$

Unfortunately, K is ill-conditioned, and regularization techniques are necessary to restore continuity of the solution back onto the data. Most regularization schemes treat all parts of K uniformly and apply Tikhonov, singular value decomposition (SVD), or Twomey algorithms with a single regularization parameter. Briefly, one wishes to find an approximate vector, $\xi_{E\varepsilon}$, that represents a balance between the residual error $\|\xi_T - K\xi_{E\varepsilon}\|$, which is corrupted by error and the ill-posed nature of the problem, and whatever side constraints we place on the solution based on *a priori* knowledge. Rather than applying the same level of regularization to the entire matrix K, we have found that it is possible, and advantageous, to first decompose K into submatrices and then apply regularization differently to each component of the resulting expression.

The rationale for such a local approach is that the discontinuities in the inverse solution appear irregularly distributed throughout the solution domain. Tikhonov and other regularization schemes are, in effect, filters, which restore continuity by attenuating the high (spatial) frequency components of the solution. Since regularization is usually applied globally, the results can leave some regions overly damped or smoothed while others remain poorly constrained. Our idea is then to apply regularization only to regions (represented by the sub-matrices of K) that require it and to apply different amounts of regularization to different sub-matrices.

We begin by expressing $K\xi_E = \xi_T$ for the Cauchy problem in (3) as

$$\begin{pmatrix} K_{TT} & K_{TV} & K_{TE} \\ K_{VT} & K_{VV} & K_{VE} \\ K_{ET} & K_{EV} & K_{EE} \end{pmatrix} \begin{pmatrix} \xi_T \\ \xi_V \\ \xi_E \end{pmatrix} = \begin{pmatrix} 0 \\ 0 \\ 0 \end{pmatrix}. \tag{65}$$

We can then rearrange the matrix to solve directly for the epicardial voltages in terms of the measured body surface voltages,

$$\xi_E = (K_{TV}K_{VV}^{-1}K_{VE} - K_{TE})^{-1}(K_{TT} - K_{TV}K_{VV}^{-1}K_{VT})\xi_T, \tag{66}$$

where the subscripts T, V, and E stand for the nodes in the regions of the torso, the internal volume, and epicardium, respectively. Since torso and epicardial nodes are always separated by more than one element, the K_{TE} submatrix is zero, and we can then rewrite (66) as

$$\xi_E = (K_{VE}^{-1} K_{VV} K_{TV}^{-1})(K_{TT} - K_{TV} K_{VV}^{-1} K_{VT})\xi_T. \qquad (67)$$

Note that we now have inverses of three sub-matrices, K_{VE}, K_{TV}, and K_{VV}, as well as several other matrix operations to perform. If one estimates the condition number, κ, of the three sub-matrices using the ratio of the maximum to minimum singular values from a SVD, one finds that the condition number varies significantly (from $\kappa \approx 200$ for K_{VV} to $\kappa \approx 1 \times 10^{16}$ for K_{VE} in the two-dimensional model described below). Thus, one can regularize each of the sub-matrices differently, even leaving some of the other sub-matrices untouched. The overall effect of this *local regularization* is more control over the regularization process.

Since the goal of the inverse problem in electrocardiography is to accurately and noninvasively (i.e., non-surgically) estimate the voltages on the epicardial surface, we need a method to choose an *a priori* optimal regularization parameter. Traditional schemes have been based on discrepancy principles [38], quasi-optimality criterion [38, 39], and generalized cross-validation [40]. Recently, Hansen [41] has extended the observations of Lawson and Hanson [42] and proposed a new method for choosing the regularization parameter based on an algorithm that locates the "corner" of a plot of the norm (or semi-norm) of the side constraint, $\|Lx_\alpha\|$, versus the norm of the corresponding residual vector, $\|Ax_\alpha - b\|$. In this way, one can evaluate the compromise between the residual error and the effect of the side constraint on the solution. We have utilized this *L-curve* algorithm along with our local Tikhonov regularization scheme to improve the accuracy of solutions to the inverse problem.

For the global Tikhonov regularization scheme, we can estimate $\xi_{E\varepsilon}$ by minimizing a generalized form of the Tikhonov functional:

$$M^\lambda[\xi_E, \tilde{\xi}_T, \tilde{K}] = \|K\xi_E - \tilde{\xi}_T\|^2_{\phi_T} + \lambda\|C(\xi_E - \xi_E^{'})\|^2_{\phi_E} \quad \lambda > 0 \quad (68)$$

in terms of the epicardial potentials,

$$\xi^\lambda_{E\varepsilon} = [\tilde{K}^T \tilde{K} + \lambda C^T C]^{-1} [\tilde{K}^T \tilde{\xi}_T + \lambda C^T C \xi_E^{'}] \qquad (69)$$

where $\tilde{K}$ is the approximation of the true transformation matrix, K, $\tilde{\xi}_T$ are the measured torso potential values, $\xi_E^{'}$ are *a priori* constraints placed on the epicardial potentials based on physiological considerations, C is a constraint matrix (either the identity matrix, a gradient operator, or a Laplacian operator), and λ is the regularization parameter. For our *local* regularization scheme, we replace the global matrix, K, by the two sub-matrices K_{VE} and K_{TV} from (67). We note that K_{VV} in (67) has a stable inverse and, thus, does not need regularizing.

Another traditional method for regularization the ill-conditioned nature of the transfer matrix is to use a truncated SVD [43]. The singular value decomposition of a matrix A is of the form

$$A = U\Sigma V^T = \sum_{i=1}^{n} u_i \sigma_i v_i^T, \tag{70}$$

where $U = (u_1, \ldots, u_n) \in R^{m\times n}$ and $V = (v_1, \ldots, v_n) \in R^{n\times n}$ are matrices with orthonormal columns, and where the diagonal matrix, $\Sigma = \text{diag}(\sigma_1, \ldots, \sigma_n)$ has non-negative diagonal elements appearing in non-decreasing order and are called the singular values of A.

Since the condition of the matrix A can be measured (in the 2-norm) in terms of the singular values

$$\text{cond}(A) \equiv \|A\|_2 \|A^{-1}\|_2 = \sigma_1/\sigma_n \tag{71}$$

one strategy for regularization is to sum the rank-one products of the singular value expansion only to a specified cut-off value $k < n$ where the singular value become "small." For the electrocardiographic inverse problem, $K\xi_E = \xi_T$, this produces a truncated summation estimate for ξ_E

$$\xi_E = K^\dagger \xi_T = \sum_{i}^{k} \frac{u_i^T \xi_T}{\sigma_i} v_i \tag{72}$$

by projecting the "good" data onto the left and right singular vectors U and V. While the truncated SVD technique provides answers comparable with Tikhonov regularization with $L = I$, it does not provide optimal results [43].

A related approach that has recently been applied to regularization of ill-conditioned systems is the generalized singular value decomposition (GSVD) in which the generalized singular values of (A, L) are essentially the square roots of the generalized eigenvalues of the matrix pair $(A^T A, L^T L)$ [16]. The GSVD is a decomposition of A and L in the form

$$A = U \begin{pmatrix} \Sigma & 0 \\ 0 & I_{n-p} \end{pmatrix} X^{-1} \tag{73}$$

and

$$L = v(M,0)X^{-1} \tag{74}$$

The columns of $U \in R^{m\times n}$ and $V \in R^{p\times p}$ are orthonormal, $X \in R^{n\times n}$ is nonsingular with columns that are A^TA-orthogonal, and Σ and M are $p \times p$ diagonal matrices: $\Sigma = \mathrm{diag}(\sigma_1,\ldots,\sigma_p)$, $M = \mathrm{diag}(\mu_1,\ldots,\mu_p)$. The *generalized* singular values γ_i of (A, L) are defined as the ratios of σ_i and μ_i

$$\gamma_i = \frac{\sigma_i}{\mu_i} \tag{75}$$

The pseudo-inverse of A in terms of the GSVD can be computed as

$$A^\dagger = X \begin{pmatrix} \Sigma^\dagger & 0 \\ 0 & I_{n-p} \end{pmatrix} U^T \tag{76}$$

such that a regularized solution can be written as

$$\xi_E = X\Phi \begin{pmatrix} \Sigma^\dagger & 0 \\ 0 & I_{n-p} \end{pmatrix} U^T \xi_T \tag{77}$$

where Φ are called the *filter factors* and depend on the amount of regularization. In this case, one would truncate the offending singular values, as well as modify the basis of the right singular vectors with the L operator. We have found that using L operators that approximate the operator of the original governing partial differential equation (in this case the Laplacian), provide the best results. However, constructing the “best” L operator is still a topic for further research.

4 Results and Discussion

To study forward and inverse problems in electrocardiography, we developed a series of two- and three-dimensional boundary element and finite element models based upon magnetic resonance images from a human subject. Each of 116 MRI scans were segmented into contours defining torso, fat, muscle, lung, and heart regions. Additional node points were added to each layer and pairs of layers tessellated into tetrahedra using a Delaunay triangulation algorithm [44, 45] at shown in Figure 1. The resulting model of the human thorax contained approximately 675,000 volume elements, each with a corresponding conductivity tensor [46]. A visualization of a forward simulation from epicardial potentials is shown in Figure 2

Figure 1: A view of the model construction process. Starting from MRI scans, the geometric model is constructed through image segmentation, triangulation of the surfaces (such as the lung), and automatic tetrahedral mesh generation.

A single (two-dimensional) layer of this model, located approximately 4 cm above the apex of the heart, as shown in Figure 3, provided a more tractable geometry for the initial studies on the effects of adaptive control of errors and local regularization.

4.1 Adaptive Meshing

Test data for the adaptive h-refinement algorithm consisted of a simulated dipolar source distribution placed on the surface of the heart model. Using the procedure described above, we computed direct solutions for different levels of mesh refinement and compared their effect on the potentials computed at the outer torso boundary. Figure 5 shows the voltage at the outer boundary versus distance around the two-dimensional contour for the original and five iterations of the adapted mesh. The original mesh contained approximately 1500 elements while the final mesh, after five iterations of the adaptive algorithm, contained approximately 7000 elements. The maximum estimated error in the calculated potential was over 30% greater in the original mesh compared to the final mesh and the maximum estimated error

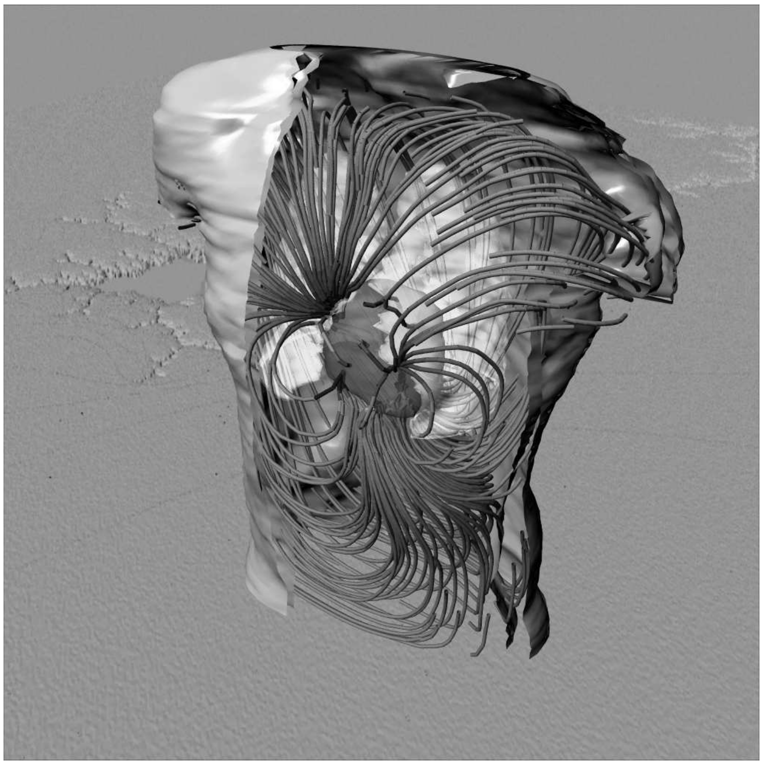

Figure 2: A visualization of the geometry and electrical current flow in a model of the human thorax for a single time step in the cardiac cycle. From Johnson.

in the potential gradient was over 13% larger in the original mesh compared to the refined mesh. Figures (6-7), show results from using the adaptive *hp* technique to compute the inverse solution. In this set of simulations, we changed the order of the basis functions on the interior (epicardial) and exterior (torso) boundaries between first order linear elements to fifth order quintic elements.

A reasonable, physically-based assumption, in utilizing adaptive methods would be that because of the higher voltage gradients near the epicardial surface, one would need to provide more "mathematical support" near the heart's surface by either doing an h-refinement (as shown in shown in Figure 4) or using an p or hp refinement by increasing the order of the basis function near the epicardial surface. Seemingly, this would create a more

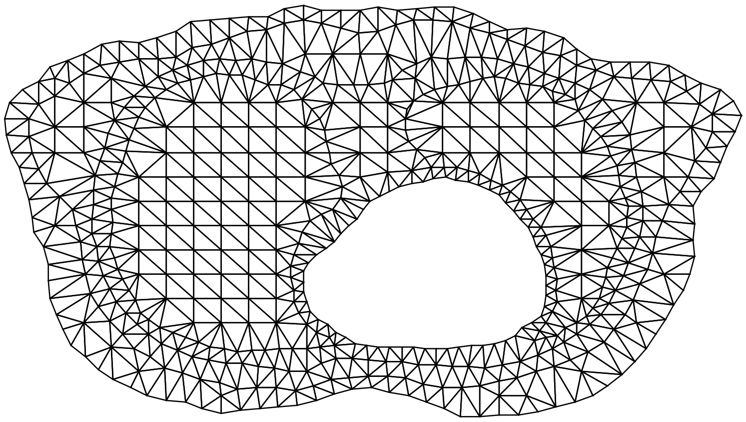

Figure 3: A triangulated MRI prior to mesh refinement that forms the basis for a finite element approximation for forward and inverse ECG solutions.

accurate “transfer matrix” and would thus produce more accurate forward and inverse solutions.

While this has been proved to be the case for forward solutions, it is not necessarily the case for ill-posed inverse problems that yield ill-conditioned transfer matrices. The increase in the number of degrees of freedom by using a simple h-refinement method near the epicardial surface seems to have to unfortunate effects on the numerical solution of the inverse ECG problem:

1. The increase in the number of degrees of freedom causes a proportional increase in the condition number of the transfer matrix.

2. Because of the ill-posed nature of the problem, the continued refinement of elements near the epicardial surface may not be having any positive effect beyond a particular level of refinement because one cannot retrieve information beyond a particular point. Furthermore, because of point one, not only is the additional refinement not providing additional useful information, it may be having a negative effect on the accuracy of the solution.

In experimenting with various orders of adaptation, we came across another interesting numerical property with regard to the inverse ECG problem, namely that increasing the order of the basis function on the outer (torso) surface increased the accuracy of the solutions. One possible expla-

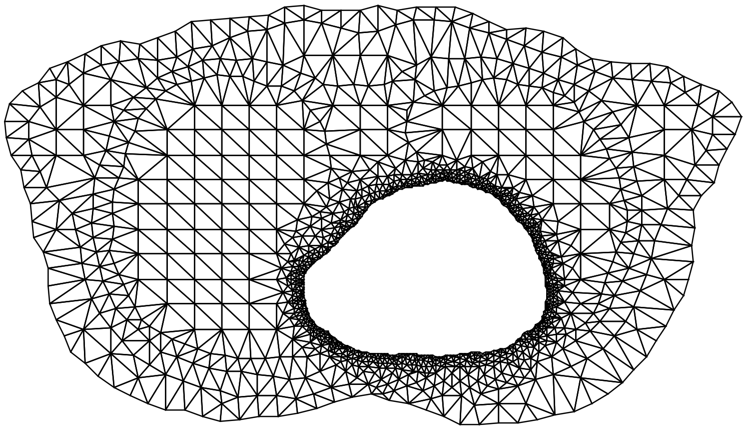

Figure 4: A triangulated MRI after two iterations of the mesh refinement algorithm. From Schimdt et al.

nation for this effect is that because of the ill-posed nature of the inverse ECG problem, small errors in the input data (torso data) can cause large errors in the solution (epicardial data). In most numerical finite element (and finite difference) implementations, one uses linear basis functions. This means that the Neumann boundary condition is approximated by a difference equation using first order methods. This can lead to significant errors when sampling over a somewhat course mesh. In using higher order basis functions at the torso boundary, we saw an improvement of the solution accuracy, possibly due to better numerical estimation of the Neumann (and Dirichlet) boundary conditions (i.e. the input data).

Figures (6-7), show results from using adaptive hp-refinement. The vertical axes denotes the epicardial voltages at one instant of time in the cardiac cycle from either the true or computed solutions. The horizontal axes denotes the node number along the epicardial contour of Figure 3. Note the difference in the RMS errors when we use a high order basis function at the epicardial surface (Figures 8 and 7) versus a higher order basis function on the torso surface (Figures 6 and 9), in which the best solution accuracy (9.1% RMS error) was observed with fifth order elements on the torso boundary and linear elements on the epicardial surface. Increased accuracy does not come without a price; the h- and hp-adaptation increases the number of degrees of freedom, and thus, the computational costs. From these initial studies, it seems clear that there are many unanswered ques-

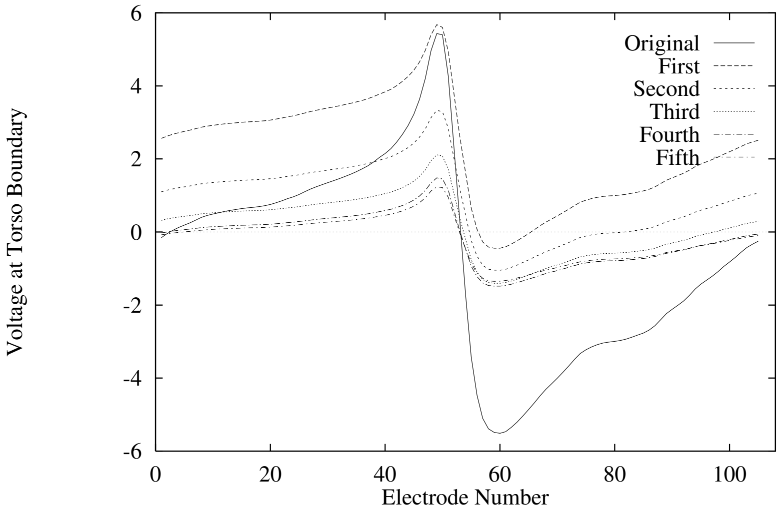

Figure 5: Effects of Automatic Mesh Refinement. The graphs shows potential value versus node number for the sequence of nodes around the outer perimeter of the two-dimensional geometry for a sequence of mesh refinements.

tions concerning the interplay between adaptive numerical techniques and the ill-posed inverse ECG problem:

- Accuracy of the inverse solution depends on:
  - The accuracy of the transfer matrix.
  - The condition of the transfer matrix.
  - The ability to restore continuity of the solution onto the data.
- In turn, the condition of the discrete problem varies with:
  - The number of degrees of freedom.
  - The correct incorporation of boundary conditions numerically.
  - The ratio of the min/max area (volume) of the elements.

Developing an adaptive strategy that is "tuned" towards ill-posed inverse problems is an open research problem, whose solution would benefit accurately computing the numerical solution of the inverse ECG problem.

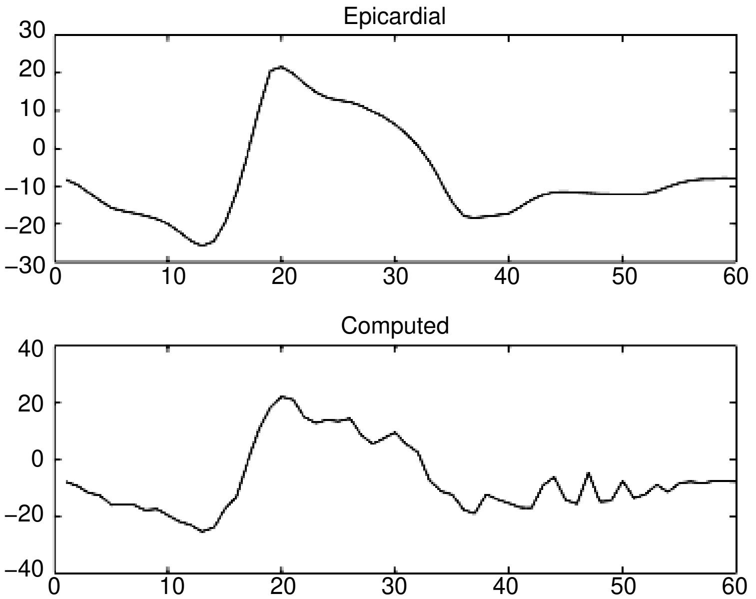

Figure 6: For this computation, third order elements were used on the outer torso boundary and linear elements were used for the interior epicardial boundary with a total of 1649 elements. There was a 16% RMS error between the true and computed solutions.

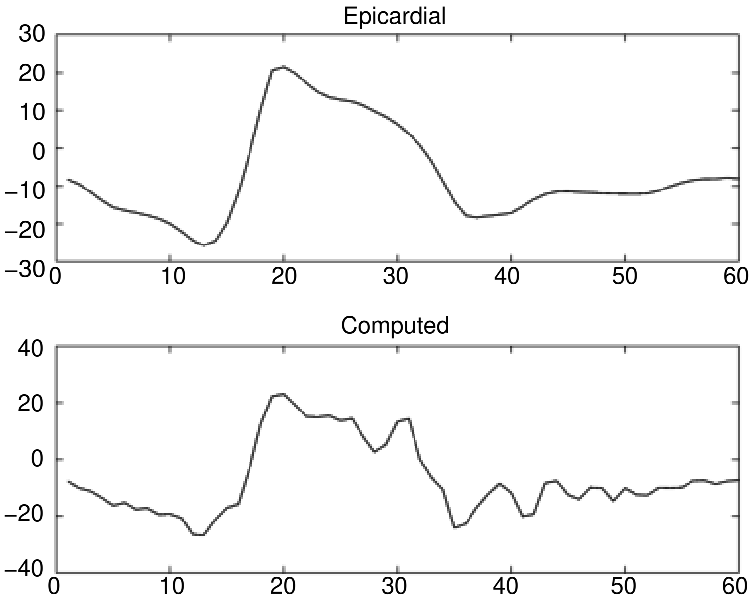

Figure 7: For this computation, first order elements were used on the outer torso boundary and third order elements were used for the interior epicardial boundary with a total of 3824 elements. There was a 23% RMS error between the true and computed solutions.

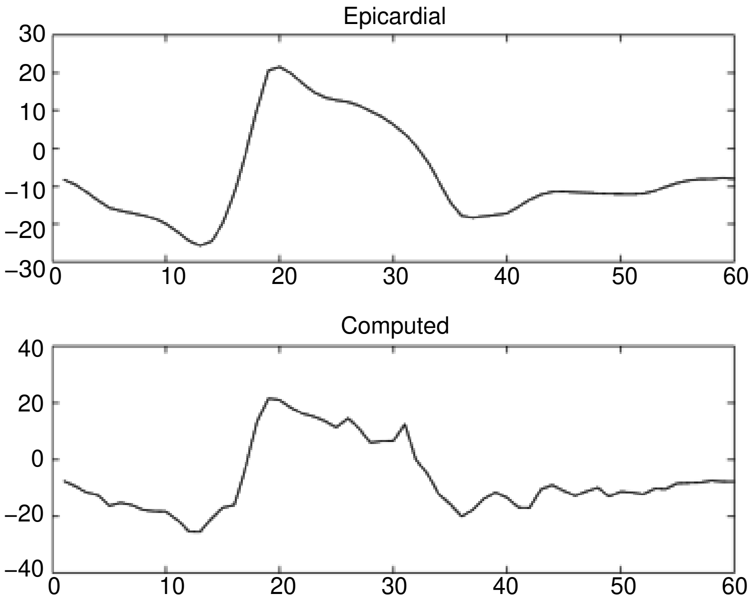

Figure 8: For this computation, third order elements were used on the outer torso boundary and third order elements were used for the interior epicardial boundary with a total of 4365 elements. There was a 15% RMS error between the true and computed solutions.

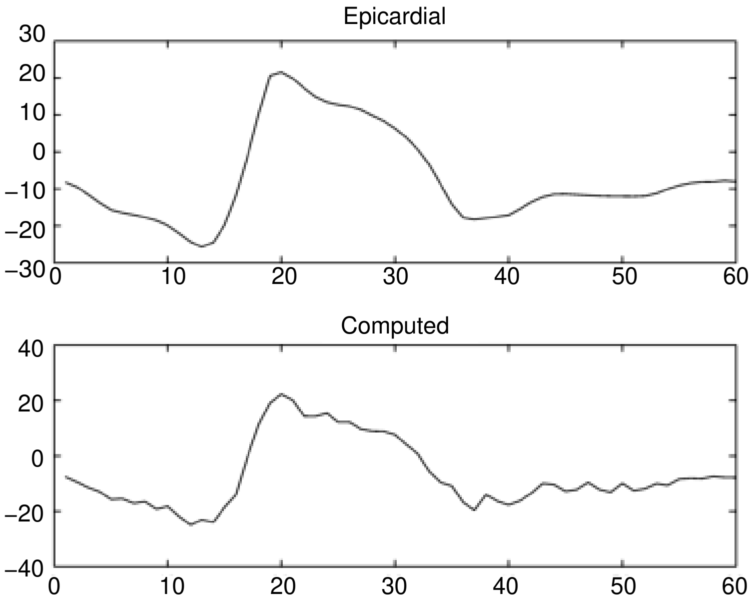

Figure 9: For this computation, fifth order elements were used on the outer torso boundary and linear elements were used for the interior epicardial boundary with a total of 3418 elements. There was a 9% RMS error between the true and computed solutions.

4.2 Local Regularization

To test the local regularization technique, we applied epicardial potentials recorded during open chest surgery from a cardiac arrhythmia patient as the Dirichlet boundary conditions of the two-dimensional model described above. The tissue conductivities were assigned as follows: fat = .045 S/m, epicardial fat-pad = .045 S/m, lungs = .096 S/m, skeletal muscle (in the fiber direction) = .3 S/m, skeletal muscle (across the fiber direction) = .1 S/m, and an average thorax value = .24 S/m. Forward solutions calculated using the adapted mesh served as torso boundary conditions, where $\Phi = \Phi_0$ on $\Sigma \subseteq \Gamma_T$ for the inverse solution both with and without 10% added Gaussian noise.

For the sub-matrices A_{VE} and A_{TV}, the *L-curve* algorithm determined the optimal *a priori* regularization parameter. The local Tikhonov regularization technique was then applied to the two sub-matrices and the inverse solution matrix computed. Because the size of the two-dimensional finite element model was relatively small, the calculations stayed in dynamic memory on an SGI Indigo2 workstation and completed within a few seconds. To evaluate the results, we compare the locally regularized inverse solutions to those from a global Tikhonov regularization as well as the known epicardial solutions.

The application of the local regularization technique with the GSVD recovered the voltages to within 6.1% relative root-mean-squared (RMS) error of the true solution. This compares with a previous best from our work of 12.1% relative error [47]. Previous studies have reported the recovery of epicardial potentials with errors in the range of 20–100%, [43, 48, 49, 50, 51, 12, 11], although in these cases investigators used three-dimensional geometric models and in some cases measured potentials on both epicardial and torso surfaces. We used another common strategy [12, 11, 14] of applying a forward solution to measured epicardial potentials in order to generate the torso potentials, which, with added noise, served as the input to the inverse procedure. Figure 10 shows the inverse solution calculated using the local regularization technique compared with the recorded heart voltages as a function of position on the epicardium. The global solution tended to be smoother, not able to follow the extrema as well as the local solution could. The local regularized solution also showed a few areas of local error which suggest that a different partitioning of the sub-matrices might provide even better accuracy. In Figures 11 we show the errors between global and local regularizations and the exact potentials.

One of the interesting effects of the GSVD-based local regularization

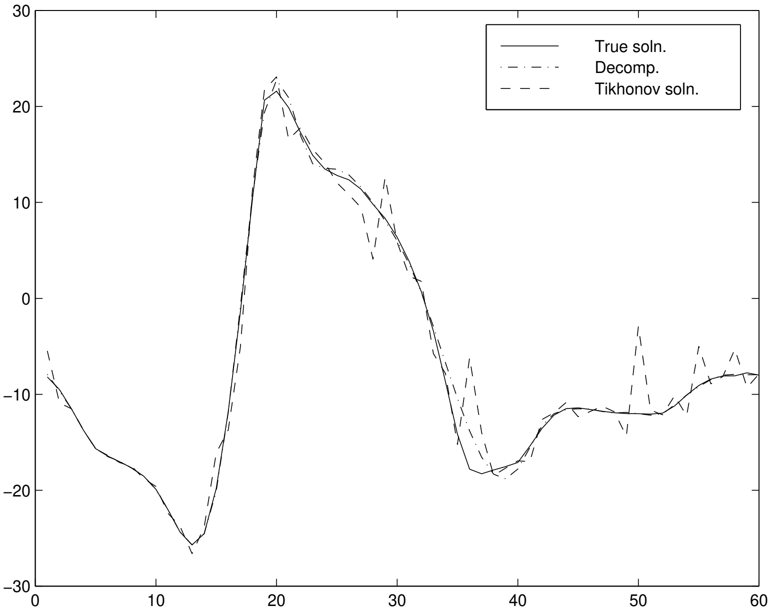

Figure 10: Local GSVD-based regularization technique. The figure shows the GSVD local regularization solution (marked Decomp), the best Tikhonov solution, and true solution.

method is its stability when random noise is added to the thorax potentials. The GSVD-based local method is affected very little by the addition of 10% Gaussian noise in sharp contrast to the effects of noise on the Tikhonov solution as shown in Figures 12 and 13 .

There have been other approaches to local regularization reported in the literature recently. Approaches that are local in time, *i.e.,* that vary the regularization parameter as a function of time step, were proposed by Iakovidis and Gulrajani [52]. Oster and Rudy have proposed a method they have named "regional regularization", in which they decomposed the body surface potential maps—the input data to the electrocardiographic inverse problem—using either Legendre polynomials or singular value decompositions for concentric and eccentric spherical geometric models for which analytic solutions exist [11]. They then applied individual regularization to components of the decomposition, producing improvements in the accuracy of the resulting inverse solution. This regional regularization technique differs from that presented here in that the link between components of the

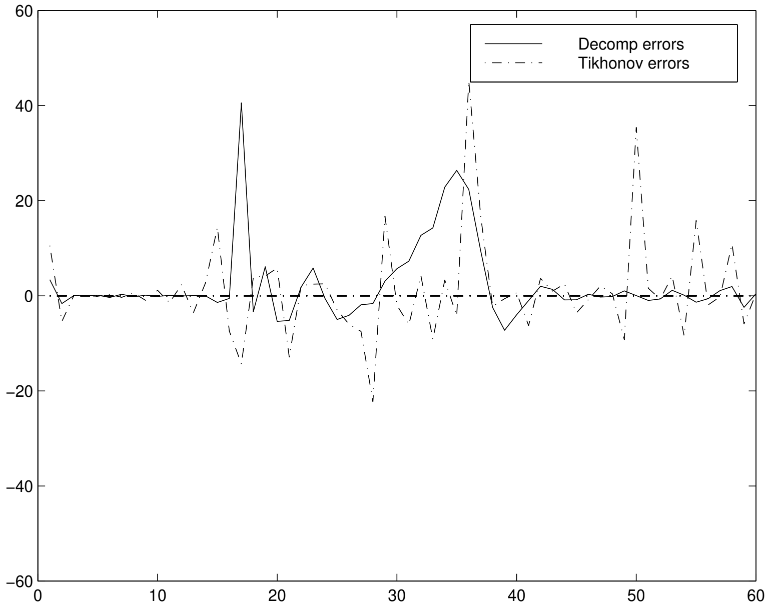

Figure 11: Errors for local and global regularization techniques. The figure shows the errors for the local solution (marked Decomp) and global Tikhonov for the solutions in the previous figures as functions of node number.

decomposition and actual regions of the geometry is only indirect—the decomposition is based on signal content and not geometry. This feature is also a strength of the regional approach in that regularization changes with the input data and their signal-to-noise ratio.

A fundamentally different approach to solving the inverse problem that also permits local weighting is that proposed by Brooks *et al.* [53, 12]. Termed the "admissible solution approach", this solution strategy does not include regularization but instead seeks to restrict the allowable solution space iteratively based an a wide variety of constraints, all applied simultaneously. In order to apply such constraints locally, a matrix based on the forward solution matrix (and hence the problem geometry) determines the weighting of each constraint on each node in the geometric model. The form of the weighting matrix can be freely selected to reflect *a priori* knowledge of the problem or made to depend on the input data. In one example, Brooks *et al.* varied the local weighting of constraints based on

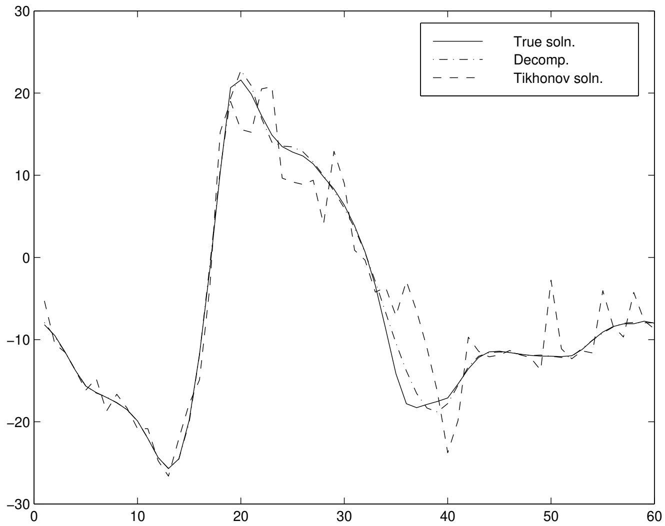

Figure 12: Effects of Noise on the GSVD and Tikhonov Solutions. Here 10% random noise has been added to torso potentials and the GSVD-based local regularization (Decomp) and Tikhonov solutions recomputed.

an estimate of the Laplacian from the (known) epicardial distributions, emphasizing the constraints in regions of small Laplacian and deemphasizing them in regions of larger Laplacian. One result was an improvement in the reconstruction of epicardial potential amplitudes. While this weighting approach is very similar to that applied here in that it is explicitly attached to the problem geometry, the admissible solutions method is fundamentally different from the Tikhonov regularization that we have used.

5 Conclusion

We have described two new strategies—adaptive finite element methods and local regularization techniques—to more accurately recover epicardial potentials from measured body surface potentials using an electrocardiographic inverse solution and discrete geometric models based on MRI. We have also described several open issues regarding the numerical solution of the inverse ECG problem, including how to accurately implement boundary conditions correctly from a numerical standpoint, how to determine the interplay between adaptive methods and the ill-posed nature of the inverse

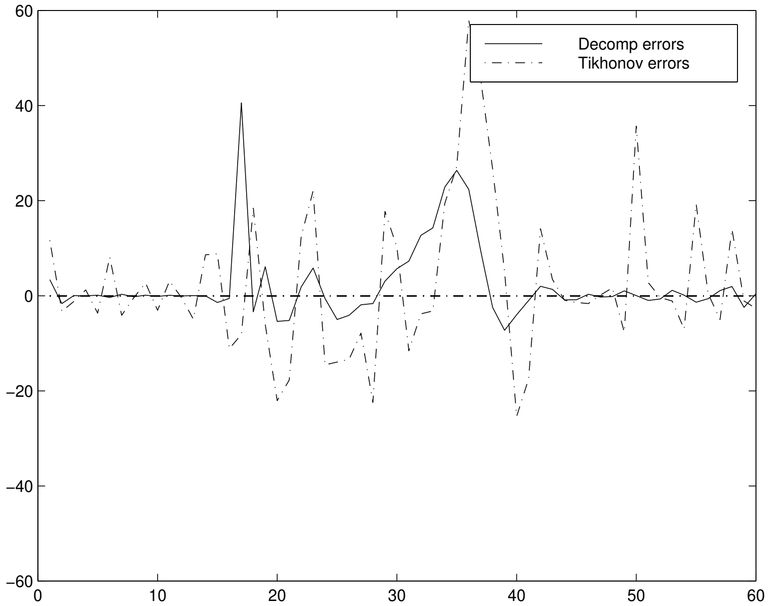

Figure 13: Errors for local and global regularization techniques with 10% added Gaussian noise. The figure shows the error as a function of node number after local (Decomp) and global Tikhonov regularization.

ECG problem, how to partition the transfer matrix so as to find the "best" partitioning for local regularization methods, and how to do all of this for large-scale problems with complicated geometry.

One idea we are pursuing for addressing the issues above, is to use a multiresolution/multigrid approach in which different amounts of regularization can be applied at different levels of the hierarchy/grid resolution. Such a multiresolution structure could address the issues of adaptive refinement, local regularization, and computational efficiency for large-scale problems.

Historically, two major challenges have impeded clinical utility of the electrocardiographic inverse solution: one of obtaining enough accuracy in the inverse solution (a generally held opinion dictates that solution accuracy less than 10% RMS error is necessary for clinical application) and the ability to compute inverse solutions in a time-efficient manner, . Recent developments of novel regularization methods like those described here suggest that major breakthroughs in numerical accuracy are within our reach. This combination will, we believe, soon lead to practical inverse solutions in medicine.

We are now pursuing the application of these methods to detailed, large-scale MRI-based thorax models, as well as head/brain models for electroencephalographic inverse problems.

6 Acknowledgments

This research was supported in part by awards from the National Science Foundation. The author would like to acknowledge Robert MacLeod's significant contribution to this work. Thanks also to Yarden Livnat for assistance with the *hp* finite element simulations and to David Weinstein for helpful comments and suggestions and help with the figures.

References

[1] R.M. Gulrajani, P. Savard, and F.A. Roberge. The inverse problem in electrocardiography: Solutions in terms of equivalent sources. *Crit. Rev. Biomed. Eng.*, 16:171–214, 1988.

[2] Y. Yamashita. Theoretical studies on the inverse problem in electrocardiography and the uniqueness of the solution. *IEEE Trans Biomed. Eng.*, BME-29:719–725, 1982.

[3] J.J.M. Cuppen. Calculating the isochrones of ventricular depolarization. *SIAM J. Sci. Statist. Comp.*, 5:105–120, 1984.

[4] G.J. Huiskamp and A. van Oosterom. The depolarization sequence of the human heart surface computed from measured body surface potentials. *IEEE Trans Biomed. Eng.*, BME-35:1047–1059, 1989.

[5] G.J. Huiskamp and A. van Oosterom. Tailored versus geometry in the inverse problem of electrocardiography. *IEEE Trans Biomed. Eng.*, BME-36:827–835, 1989.

[6] Y. Rudy and B.J. Messinger-Rapport. The inverse solution in electrocardiography: Solutions in terms of epicardial potentials. *Crit. Rev. Biomed. Eng.*, 16:215–268, 1988.

[7] R.M. Gulrajani, F.A. Roberge, and G.E. Mailloux. The forward problem of electrocardiography. In P.W. Macfarlane and T.D. Veitch Lawrie, editors, *Comprehensive Electrocardiology*, pages 197–236. Pergamon Press, Oxford, England, 1989.

[8] R.M. Gulrajani, F.A. Roberge, and P. Savard. The inverse problem of electrocardiography. In P.W. Macfarlane and T.D. Veitch Lawrie, editors, *Comprehensive Electrocardiology*, pages 237–288. Pergamon Press, Oxford, England, 1989.

[9] I. Iakovidis and C.F. Martin. A model study of instability of the inverse problem of electrocardiography. *Mathematical Biosciences*, 107:127–148, 1991.

[10] C.R. Johnson and R.S. MacLeod. Local regularization and adaptive methods for the inverse Laplace problem. In D.N. Ghista, editor, *Biomedical and Life Physics*, pages 224–234. Vieweg-Verlag, Braunschweig, 1996.

[11] H.S. Oster and Y. Rudy. Regional regularization of the electrocardiographic inverse problem: A model study using spherical geometry. *IEEE Trans Biomed. Eng.*, 44(2):188–199, 1997.

[12] G.F. Ahmad, D. H Brooks, and R.S. MacLeod. An admissible solution approach to inverse electrocardiography. *Annal. Biomed. Eng.*, 26:278–292, 1998.

[13] D.H. Brooks, G. Ahmad, and R.S. MacLeod. Multiply constrained inverse electrocardiology: Combining temporal, multiple spatial, and iterative regularization. In *Proceedings of the IEEE Engineering in Medicine and Biology Society 16th Annual International Conference*, pages 137–138. IEEE Computer Society, 1994.

[14] D.H. Brooks, G.F. Ahmad, R.S. MacLeod, and G.M. Maratos. Inverse electrocardiography by simultaneous imposition of multiple constraints. *IEEE Trans Biomed. Eng.*, 46(1):3–18, 1999.

[15] P.C. Hansen. Analysis of discrete ill-posed problems by means of the L-curve. *SIAM Review*, 34(4):561–580, 1992.

[16] P.C. Hansen. *Rank-Deficient and Discrete Ill-Posed Problems: Numerical aspects of linear inversion*. PhD thesis, Technical University of Denmark, 1996.

[17] R.S. MacLeod and D.H. Brooks. Recent progress in inverse problems in electrocardiology. *IEEE Eng. in Med. & Biol. Soc. Magazine*, 17(1):73–83, January 1998.

[18] R.S. MacLeod, R.M. Miller, M.J. Gardner, and B.M. Horáček. Application of an electrocardiographic inverse solution to localize myocardial ischemia during percutaneous transluminal coronary angioplasty. *J. Cardiovasc. Electrophysiol.*, 6:2–18, 1995.

[19] H.S. Oster, B. Taccardi, R.L. Lux, P.R. Ershler, and Y. Rudy. Noninvasive electrocardiographic imaging: Reconstruction of epicardial potentials, electrograms, and isochrones and localization of single and multiple electrocardiac events. *Circ.*, 96(3):1012–1024, 1997.

[20] C.J. Penney, J.C. Clements, M.J. Gardner, L. Sterns, and B.M. Horáček. The inverse problem of electrocardiography: application to localization of Wolff-Parkinson-White pre-excitation sites. In *Proceedings of the IEEE Engineering in Medicine and Biology Society*

17th Annual International Conference, pages 215–216. IEEE Press, 1995.

[21] D.S. Burnett. *Finite Element Method*. Addison Wesley, Reading, Mass., 1988.

[22] C. Johnson. *Numerical solution of Partial Differential Equations by the Finite Element Method*. Cambridge University Press, Cambridge, 1990.

[23] G. Strang and G. Fix. *An Analysis of the Finite Element Method*. Prentice–Hall, Englewood Cliffs, NJ, 1973.

[24] B. Szabó and I. Babuška. *Finite Element Analysis*. John Wiley & Sons, New York, 1991.

[25] C.R. Johnson and R.S. MacLeod. Nonuniform spatial mesh adaptation using a posteriori error estimates: applications to forward and inverse problems. *Applied Numerical Mathematics*, 14:311–326, 1994.

[26] J.A. Schmidt, C.R. Johnson, J.C. Eason, and R.S. MacLeod. Applications of automatic mesh generation and adaptive methods in computational medicine. In I. Babuska, J.E. Flaherty, W.D. Henshaw, J.E. Hopcroft, J.E. Oliger, and T. Tezduyar, editors, *Modeling, Mesh Generation, and Adaptive Methods for Partial Differential Equations*, pages 367–390. Springer-Verlag, 1995.

[27] P.G. Ciarlet and J.L Lions. *Handbook of Numerical Analysis: Finite Element Methods*, volume 1. North-Holland, Amsterdam, 1991.

[28] R. Rannacher and R. Scott. Some optimal error estimates for piecewise linear finite element approximations. *Math. Comp.*, 38:437–445, 1982.

[29] L. Demkowicz, J.T. Oden, W. Rachowicz, and O. Hardy. Toward a universal h-p adaptive finite element strategy, Part 1. Constrained approximation and data structure. *Computaitonal Methods in Applied Mechanical Engineering*, 77:79, 1989.

[30] J.T. Oden, L. Demkowicz, W. Rachowicz, and O. Hardy. Toward a universal h-p adaptive finite element strategy, Part 2. A posteriori error estimation. *Computaitonal Methods in Applied Mechanical Engineering*, 77:113, 1989.

[31] W. Rachowicz, J.T. Oden, and L. Demkowicz. Toward a universal h-p adaptive finite element strategy, Part 3. Design of h-p meshes. *Computaitonal Methods in Applied Mechanical Engineering*, 77:181, 1989.

[32] S.P. Sherwin and E.M. Karniakakis. A new triangular and tetrahedral basis for high-order (hp) finite element methods. *International Journal for Numerical Methods in Engineering*, 38:3775–3802, 1995.

[33] E.M. Karniakakis and S.P. Sherwin. *Spectral/hp Element Methods for CFD*. Oxford University Press, Oxford, UK, 1999.

[34] J.E. Flaherty. *Adaptive Methods for Partial Differential Equations*. SIAM, Philadelphia, 1989.

[35] O.C. Zienkiewicz and J.Z. Zhu. A simple error estimate and adaptive procedure for practical engineering analysis. *Int. J. Num. Meth. Eng.*, 24:337–357, 1987.

[36] O.C. Zienkiewicz and J.Z. Zhu. Adaptivity and mesh generation. *Int. J. Num. Meth. Eng.*, 32:783–810, 1991.

[37] I. Babuška. Error bounds for the finite element method. *Numer. Math.*, 16:322–333, 1971.

[38] V.A. Morozov. *Methods for Solving Incorrectly Posed Problems*. Springer-Verlag, New York, 1984.

[39] R. Kress. *Linear Integral Equations*. Springer-Verlag, New York, 1989.

[40] G.H. Golub, M.T. Heath, and G. Wahba. Generalized cross-validation as a method for choosing a good ridge parameter. *Technometrics*, 21:215–223, 1979.

[41] P.C. Hansen. Analysis of discrete ill-posed problems by means of the L-curve. *SIAM Review*, 34(4):561–580, 1992.

[42] C.L. Lawson and R.J. Hanson. *Solving Least Squares Problems*. Prentice-Hall, Englewood Cliffs, NJ, 1974.

[43] R.D. Throne, L.G. Olson, T.J. Hrabik, and J.R. Windle. Generalized eigensystem techniques for the inverse problem of electrocardiography applied to a realistic heart-torso geometry. *IEEE Trans Biomed. Eng.*, 44(6):447, 1997.

[44] C.R. Johnson, R.S. MacLeod, and P.R. Ershler. A computer model for the study of electrical current flow in the human thorax. *Computers in Biology and Medicine*, 22(3):305–323, 1992.

[45] C.R. Johnson, R.S. MacLeod, and M.A. Matheson. Computer simulations reveal complexity of electrical activity in the human thorax. *Comp. in Physics*, 6(3):230–237, May/June 1992.

[46] K.R. Foster and H.P. Schwan. Dielectric properties of tissues and biological materials: A critical review. *Critical Reviews in Biomed. Eng.*, 17:25–104, 1989.

[47] C.R. Johnson and R.S. MacLeod. Inverse solutions for electric and potential field imaging. In R.L. Barbour and M.J. Carvlin, editors, *Physiological Imaging, Spectroscopy, and Early Detection Diagnostic Methods*, volume 1887, pages 130–139. SPIE, 1993.

[48] P. Colli Franzone, G. Gassaniga, L. Guerri, B. Taccardi, and C. Viganotti. Accuracy evaluation in direct and inverse electrocardiology. In P.W. Macfarlane, editor, *Progress in Electrocardiography*, pages 83–87. Pitman Medical, 1979.

[49] P. Colli Franzone, L. Guerri, S. Tentonia, C. Viganotti, S. Spaggiari, and B. Taccardi. A numerical procedure for solving the inverse problem of electrocardiography. Analysis of the time-space accuracy from *in vitro* experimental data. *Math. Biosci.*, 77:353, 1985.

[50] B.J. Messinger-Rapport and Y. Rudy. Regularization of the inverse problem in electrocardiography: A model study. *Math. Biosci.*, 89:79–118, 1988.

[51] P.C. Stanley, T.C. Pilkington, and M.N. Morrow. The effects of thoracic inhomogeneities on the relationship between epicardial and torso potentials. *IEEE Trans Biomed. Eng.*, BME-33:273–284, 1986.

[52] I. Iakovidis and R.M. Gulrajani. Regularization of the inverse epicardial solution using linearly constrained optimization. In *Proceedings of the IEEE Engineering in Medicine and Biology Society 13th Annual International Conference*, pages 698–699. IEEE Press, 1991.

[53] G.F. Ahmad, D.H. Brooks, C.A. Jacobson, and R.S. MacLeod. Constraint evaluation in inverse electrocardiography using convex optimization. In *Proceedings of the IEEE Engineering in Medicine and*

Biology Society 17th Annual International Conference, pages 209–210. IEEE Press, 1995.